Journal of Materials Chemistry A

COMMUNICATION

View Article Online
View Journal | View Issue

Cite this: J. Mater. Chem. A, 2017, 5, 6832

Received 7th February 2017
Accepted 20th March 2017

DOI: 10.1039/c7ta01171g

rsc.li/materials-a

A high strength, free-standing cathode constructed by regulating graphitization and the pore structure in nitrogen-doped carbon nanofibers for flexible lithium–sulfur batteries†

Xiong Song,[a] Suqing Wang,*[ab] Yue Bao,[a] Guoxue Liu,[a] Wenping Sun,*[b] Liang-Xin Ding,[a] Huakun Liu[b] and Haihui Wang *[a]

We demonstrate here a novel strategy to prepare a flexible and free-standing sulfur cathode with improved mechanical strength, the matrix of which is constructed from graphitized nitrogen-doped mesoporous carbon nanofibers (NPCFs). Benefiting from a unique micro/mesoporous structure and highly graphitic carbon, the NPCF film is capable of accommodating more sulfur, and maintains substantially higher mechanical strength and flexibility after sulfur loading as compared with traditional microporous carbon nanofiber films. As a free-standing and flexible cathode for Li–S batteries, the robust composite film exhibits excellent rate capability (540 mA h g^{-1} at 5C) and cycling stability (76.5% retention after 500 cycles at 5C).

Introduction

With the rapidly increasing demand for electrical vehicles (EVs), portable electronic devices, and grid energy storage, ever-increasing research attention has been focused on developing high-energy, high-power and durable rechargeable batteries. The further development of traditional lithium ion batteries (LIBs) has been severely hindered by their insufficient cathode capacity, which has become a bottleneck for achieving high-energy LIBs.[1,2] Li–S batteries have attracted significant attention as a promising alternative rechargeable battery due to their high theoretical capacity (1675 mA h g^{-1}), high energy density (~2500 W h kg^{-1}), low cost, and environmentally friendly characteristics.[3–5] However, there are still many challenges to be overcome for the commercialization of Li–S batteries. Firstly, the poor electronic conductivity of elemental sulfur (~1×10^{-30} S cm^{-1} at room temperature), as well as of the discharge product Li_2S, limits the utilization of sulfur electrodes.[6] Secondly, the lithium polysulfide intermediates formed from the cathode reaction are soluble in organic electrolytes and would deposit on lithium metal electrodes, which causes active material loss and shuttle effects.[6–8] The third one is the large volume change of sulfur electrodes during the charge/discharge process. All of these issues would lead to low coulombic efficiency, fast capacity decay, inferior rate performance and safety concerns. Various attempts are being made to solve these problems, including rational design of electrode materials, separator modification, and introducing electrolyte additives and multifunctional binders.[9–15]

On the other hand, due to the emerging flexible displays and wearable electronics, mechanically robust flexible rechargeable batteries are urgently required.[16–19] A good flexible electrode should have high tensile strength which makes the electrode resistant to cracking under repeated bending. However, conventional battery electrodes cannot meet such strict requirements due to the poor flexibility and weak adhesion between the active materials and the metal foil substrates, which would lead to pulverization of active materials and thereby performance degradation during repeated bending. Carbon cloth, carbonate cellulose and textiles have been mostly used to fabricate flexible electrodes, and show good mechanical strength and flexibility.[18–22] However, the heavy mass of the flexible substrates and the low mass loading would lower the energy density of the electrodes dramatically. Free-standing electrodes should be a great choice to enhance the energy density of flexible batteries.[23–25] Vacuum filtration is widely used to fabricate flexible electrodes, which generally deploys graphene or CNTs as the matrix.[26–29] Compared with vacuum filtration, electrospinning has been extensively investigated for preparing free-standing porous carbon nanofiber films by virtue of its simplicity, low cost and scale-up potential.[30–34] Unfortunately, most of the reports on free-standing flexible electrodes merely showed digital photos of simple bending. Very few flexible films synthesized by electrospinning were reported with mechanical strength testing, but showed low breaking stress (usually lower than 2 MPa with 0.5–1.5% strain), which cannot meet the demands of practical applications.[34–38] For sulfur-based cathodes for Li–S batteries, porous

[a]School of Chemistry & Chemical Engineering, South China University of Technology, Guangzhou 510640, China. E-mail: cesqwang@scut.edu.cn; hhwang@scut.edu.cn

[b]Institute of Superconducting & Electronic Materials, Australian Institute of Innovative Materials, University of Wollongong, NSW 2522, Australia. E-mail: wenping@uow.edu.au

† Electronic supplementary information (ESI) available. See DOI: 10.1039/c7ta01171g

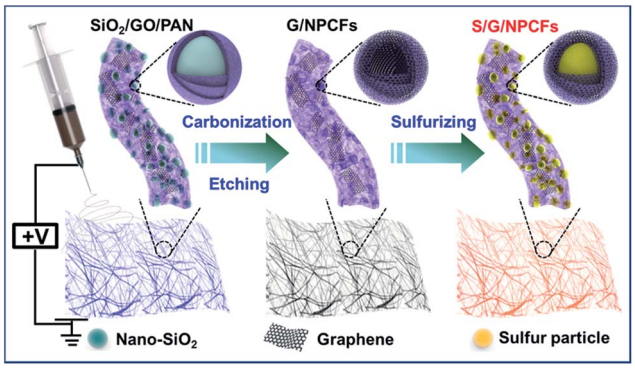

Scheme 1 Schematic illustration of the fabrication process of the S/G/NPCF composite.

carbon nanofibers are usually used to confine the sulfur. Basically, filling rigid sulfur into the micropores of the carbon nanofibers would degrade the flexibility and is detrimental to the structural stability of the flexible film. Therefore, it is still a great challenge to fabricate a stable flexible cathode with high sulfur loading and high mechanical strength for Li–S batteries.

Herein, we demonstrate a novel strategy to prepare a flexible and free-standing sulfur cathode with high mechanical strength by introducing graphitic carbon and hierarchical pores in nitrogen-doped carbon nanofibers. The fabrication procedure is illustrated in Scheme 1. Graphene oxide (GO), nano-silica (SiO_2) and polyacrylonitrile (PAN) are first mixed in *N*,*N*-dimethylformamide (DMF) for electrospinning to obtain the nanofiber film precursor (SiO_2/GO/PAN; detailed information on the as-prepared samples' abbreviations is provided in Table S1†). After carbonization and template etching of the as-collected SiO_2/GO/PAN film, a graphene-modified porous film constructed from micro/mesoporous carbon nanofibers (G/NPCFs) is successfully fabricated. Notably, highly graphitic carbon zones are formed around the SiO_2 spheres during carbonization which greatly help to improve the electrical conductivity and mechanical strength of the film. Finally, the G/NPCF film is loaded with sulfur after immersion in sulfur solution, eventually obtaining the sulfur encapsulated G/NPCF film (S/G/NPCF) after drying. The free-standing S/G/NPCF film with high sulfur loading exhibits excellent flexibility and mechanical strength, and delivers exceptional electrochemical performances (540 mA h g^{-1} at 5C with 76.5% retention after 500 cycles) as a cathode for flexible Li–S batteries.

Experimental

Materials synthesis

Preparation of flexible SiO_2/GO/PAN nanofibers. The graphene oxide (GO) used in this work was synthesized by the Hummers' method, and the detailed processes can be found in our previous work.[39] Polyacrylonitrile (PAN, M_w = 150 000, Sigma-Aldrich) and *N*,*N*-dimethylformamide (DMF, Aladdin Co. Ltd, China) were used as the carbon precursor and solvent, respectively. Nano-silica (SiO_2, 15 nm, Aladdin Co. Ltd, China) was used as the pore-forming template. Firstly, the as-prepared GO powder (5 mg mL^{-1}) and SiO_2 (20 mg mL^{-1}) were dispersed in 10 mL DMF solution and sonicated for 4 hours. Secondly, 1 g PAN was added into the above solution, followed by constant stirring at 50 °C for at least 12 hours. Finally, the above solution was loaded into a 10 mL syringe with a 20-gauge blunt tip. The electrospinning process was carried out at an applied voltage of 13–14 kV. The flow rate and tip collector distance were fixed at 1.2 mL h^{-1} and 14 cm, respectively.

Preparation of flexible S/G/NPCFs. The flexible SiO_2/GO/PAN nanofibers were first stabilized at 250 °C in air for 3 h,[32,40,41] followed by carbonization at 1000 °C for 2 h under an Ar/H_2 atmosphere. The carbonized nanofibers were further etched with 10% hydrofluoric acid (HF). Sublimed sulfur was dissolved in CS_2 solvent with a concentration of 40 mg mL^{-1} of sulfur solution. Then, the as-prepared G/NPCF composite was cut into small pieces (2.5 cm × 5 cm) and then immersed in the sulfur solution for 10 min and dried at 60 °C in an oven for 4 hours. Finally, the above sulfur-nanofiber composite was transferred to an autoclave under an argon atmosphere and heated to 155 °C for 10 h to obtain the S/G/NPCFs.

Structural characterization

The crystal structure and morphology of the as-prepared products were characterized on a Bruker D8 Advance X-ray diffractometer using filtered Cu-Kα radiation and field emission scanning electron microscope (SEM, NOVA NANOSEM 430). The microstructures of the as-prepared products were observed by transmission electron microscopy (TEM, JEM-2010HR). X-ray photoelectron spectroscopy (XPS) analysis was performed on an ESCALAB 250 X-ray photoelectron spectrometer using an Al Kα X-ray source. All XPS spectra were calibrated using the C 1s line at 284.6 eV. The mechanical strength was tested using an Instron 5565. The specific surface area was measured using the Brunauer–Emmett–Teller (BET) method (Micromeritics analyzer ASAP 2460 (USA)) at liquid nitrogen temperature, and pore size distribution (PSD) curves were obtained using the density functional theory (DFT) method (Micromeritics). The thermogravimetric (TG) curves of the precursors were collected on a NETZSCH STA44C in the temperature range from 25 to 900 °C in a nitrogen (N_2) atmosphere with a heating rate of 10 °C min^{-1}. Raman measurements were performed using a LabRAM Aramis Raman spectrometer with a laser wavelength of 532 nm.

Electrochemical measurements

The flexible and binder-free S/G/NPCF films were cut into small pieces (1.0 cm × 1.0 cm) and then directly used as working electrodes. The electrochemical performance was measured using CR2025 coin cells assembled in an argon-filled glovebox. 1 M lithium bis(trifluoromethanesulfonyl)imide (LITFSI) in a mixture of 1,2-dimethoxyethane (DME) and 1,3-dioxolane (DOL) (1 : 1 by volume) containing lithium nitrate ($LiNO_3$, 1 wt%) was used as the electrolyte, Celgard-2400 as the separator, and Li metal foil as the counter and the reference electrode. The areal sulfur loading on each electrode was about 1.1 mg cm^{-2}, and the electrolyte volume in each cell was around 40 μL. Cyclic voltammetry (CV) measurements were carried out on an electrochemical workstation (CHI760D, Chenhua Instrument

Company, Shanghai, China) over the potential range of 1.7–2.6 V *vs.* Li/Li^+ at a scan rate of 0.2 mV s^{-1}. The galvanostatic discharge–charge performance and the rate performance were tested using a Battery Testing System (Neware Electronic Co., China) from 1.7 to 2.6 V. The overpotential is based on the potential differences between the discharge–charge voltage plateaus at half capacity. All coin cells were activated at 0.1C for three cycles (1C = 1675 mA g^{-1}), and the capacity values were calculated based on the mass of sulfur. A pouch cell was assembled with the same components as the coin cell except for the Al-plastic film package. The separator and electrolyte were sandwiched between the carbon nanofiber film and Li metal foil, and then sealed with a flexible Al-plastic film. The diameter of the sulfur cathode assembled in the pouch cell was about 2.0 cm × 2.0 cm, and the electrolyte volume in each pouch was around 200 μL.

Results and discussion

The free-standing SiO_2/G/NPCF film maintains a stable smooth surface without any pulverization after carbonization, but shrinks around 20% in size as compared with the fresh SiO_2/GO/PAN composite film (Fig. 1a). As shown in Fig. 1b and c, the diameter of the nanofibers before and after carbonization is similar (about 400 nm). The structural stability of the nanofibers and film is ascribed to the presence of the graphene and the rigid SiO_2 nanoparticles, which help to stabilize the nanofibers during carbonization. But if the concentration of SiO_2 in the spinning solution increases to 30 mg mL^{-1}, the electrospinning nanofibers will become non-uniform and show some beads among the nanofibers (Fig. S1†), which severely damages the nanostructure of the nanofibers and decreases the mechanical strength of the film. The G/NPCFs feature a large amount of mesopores on the surface of the nanofibers. The broad and flat peak in the X-ray diffraction (XRD) pattern of S/G/NPCFs corresponds to the (002) plane of graphitic carbon with a low degree of graphitization (Fig. S2†).[42] The sharp diffraction peaks along the broad graphitic (002) peak prove the existence of crystallized sulfur in the S/G/NPCF film. Fig. 1d and e show that the S/G/NPCFs present a porous fibrous morphology and a certain amount of mesopores still exist after sulfur loading, which is beneficial to electrolyte permeation, acceleration of ion diffusion, and the alleviation of the large volume changes during the charge–discharge process. And no bulk sulfur particles can be found on the surface of S/G/NPCFs, indicating the homogeneous distribution of S inside the carbon fiber framework. The

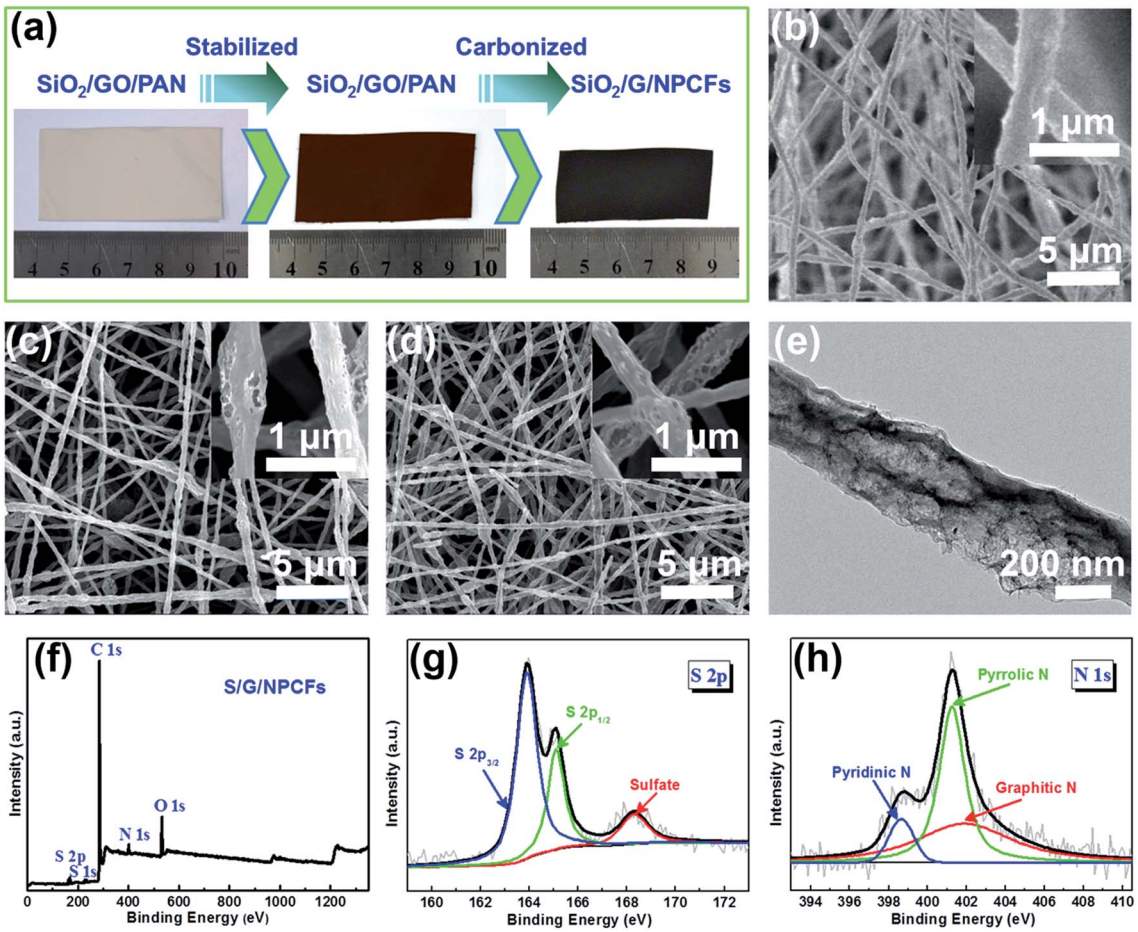

Fig. 1 (a) The photographs of the calcination process of the as-prepared film; (b) typical SEM images of GO/SiO_2/PAN, (c) G/NPCFs and (d) S/G/NPCFs; (e) TEM image of S/G/NPCFs. (f) XPS spectrum of S/G/NPCFs; high resolution spectra of (g) S 2p and (h) N 1s of S/G/NPCFs.

elemental mapping of S/G/NPCFs (Fig. S3†) further confirms that the sublimed S and nitrogen are uniformly distributed.

The X-ray photoelectron spectroscopy (XPS) of the S/G/NPCF composite shows four obvious peaks corresponding to S 2p, C 1s, N 1s and O 1s (Fig. 1f).[43] The high resolution spectra of S 2p (Fig. 1g) show two strong peaks centered at 163.9 eV and 165.1 eV, which correspond to S $2p_{3/2}$ and S $2p_{1/2}$, respectively.[44,45] The minor peak centered at 168.3 eV arises from the sulphate species due to the oxidation of sulfur during the preparation process.[46] The S content on the surface of S/G/NPCFs estimated from the XPS result is merely 1.38%, further demonstrating that most of the sublimed S is encapsulated in the internal pores of the G/NPCFs. The high resolution N 1s peak can be fitted into three peaks centered at 398.6, 401.2, and 401.9 eV, corresponding to pyridinic N, pyrrolic N, and graphitic N, respectively (Fig. 1h).[47] The percent of nitrogen atoms in the S/G/NPCF composite is about 3.07 wt%. It was proved that strong interactions can occur between lithium polysulfides and pyridinic N or pyrrolic N *via* the N lone-pair electrons, which can alleviate the dissolution of lithium polysulfides in the electrolyte, thereby improving the electrochemical performance.[48]

The structural integrity of S/G/NPCFs is well sustained after sulfur loading. As shown in Fig. 2a and Video S1 and S2,† the S/G/NPCF film could fully recover to its initial state after repeated rolling or folding into small sizes, indicating its excellent flexibility and high mechanical strength. Such superior flexibility of S/G/NPCFs gives them a great advantage for application in flexible batteries. In comparison, nitrogen-doped carbon nanofibers (NCFs) and graphene-embedded nitrogen-doped carbon nanofibers (G/NCFs) without adding the SiO_2 template are much more brittle and fracture easily during folding. The mechanical strength is closely related to the flexibility of the composite film. We further measured the mechanical properties of the obtained sulfur-containing composite films (Fig. 2b). The composite films (length = 23 mm, width = 20 mm, and thickness = 50 μm) were stretched at a speed of 1 mm min^{-1} until the films broke. The breaking stress of the sulfur encapsulated nitrogen-doped carbon nanofibers (S/NCFs) is only

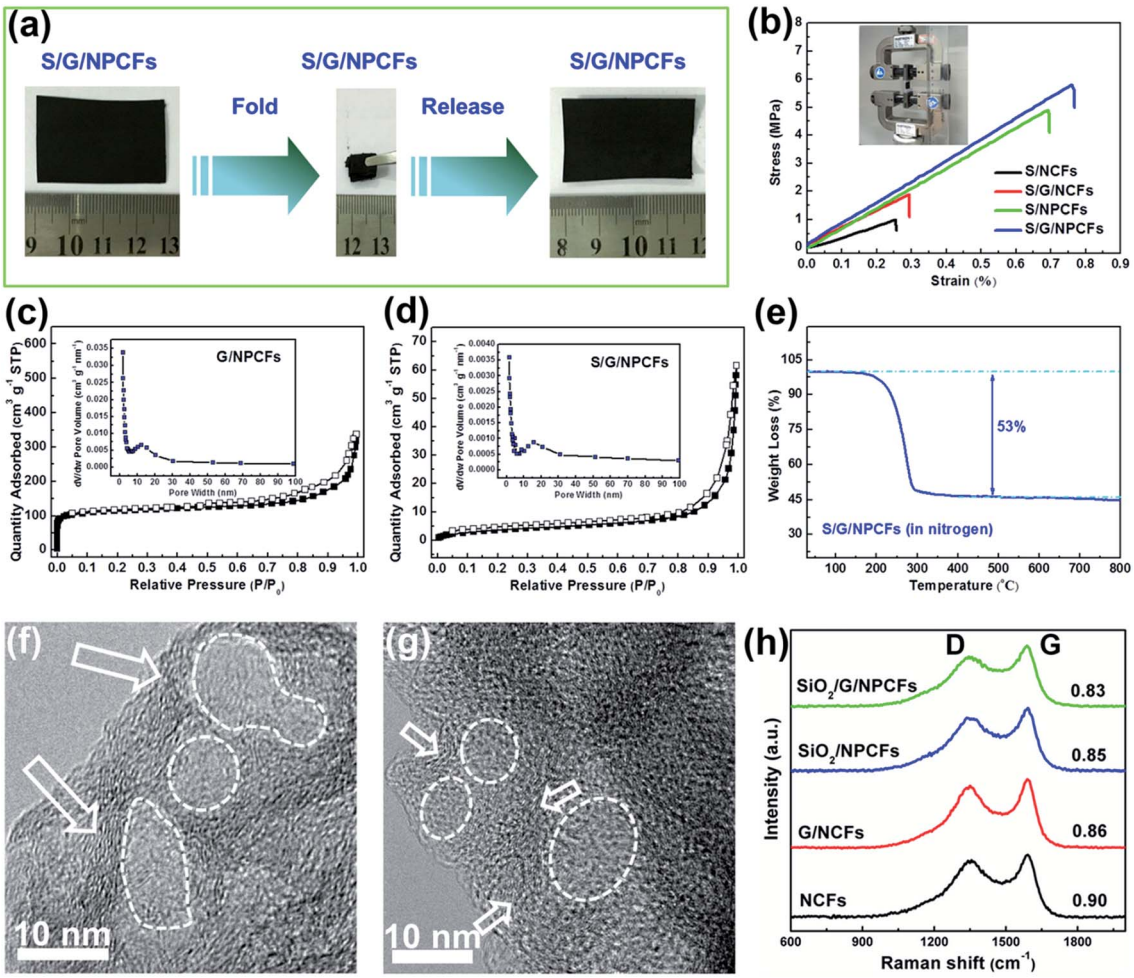

Fig. 2 (a) The photographs of the flexible and foldable S/G/NPCF composite film; (b) typical tensile stress–strain curves of the as-prepared carbon films (the inset is the photograph of the tensile stress–strain testing instrument); (c) nitrogen adsorption–desorption isotherms of G/NPCFs and (d) S/G/NPCFs (the insets are the corresponding pore size distribution curves); (e) TG curve of S/G/NPCFs (in nitrogen); (f) HRTEM of G/NPCFs; (g) HRTEM of S/G/NPCFs; (h) Raman spectra of the NCFs, G/NCFs, SiO_2/NPCFs and SiO_2/G/NPCFs (the corresponding I_D/I_G ratios are shown on the right).

1.00 MPa, while the tensile stress of the sulfur encapsulated graphene-embedded nitrogen-doped carbon nanofibers (S/G/NCFs) is improved to 1.89 MPa. More impressively, the tensile stress of S/NPCFs and S/G/NPCFs with mesopores created by the SiO_2 template is significantly enhanced and the values achieved are as high as 4.91 and 5.81 MPa, respectively, which are more than three times as high as those obtained without using the SiO_2 template. Notably, the present superior mechanical strength is also much higher than those of most of the carbon-based films reported in the literature (Fig. S4†).[34–38] The robust S/G/NPCF structure with such high mechanical strength lays a solid foundation for delivering durable performance for flexible batteries.

In order to explore the reasons for the exceptional flexibility and greatly improved mechanical strength, the microstructure of the composite film was further characterized. The NCFs show a Brunauer–Emmett–Teller (BET) surface area of 577 $m^2\ g^{-1}$ with a large micropore volume (0.227 $cm^3\ g^{-1}$), which accounts for around 82% and mainly results from the large shrinkage of the polymer during carbonization (Fig. S5a and Table S2†). It has to be mentioned that the NCFs have no obvious mesopores based on the nitrogen adsorption–desorption isotherms. The BET surface area of SiO_2/G/NPCFs decreases to 232 $m^2\ g^{-1}$ and they possess a much lower micropore volume (0.093 $cm^3\ g^{-1}$) (Fig. S5b†). The introduction of rigid SiO_2 and graphene could sustain the skeletal structure of the nanofibers during thermal treatment and help to reduce micropore volume. After removing the template, the G/NPCFs show an increased specific surface area of 429 $m^2\ g^{-1}$ with a larger total pore volume of 0.522 $cm^3\ g^{-1}$, while the micropore volume only accounts for 33% (Fig. 2c). Basically, the micropores and mesopores in the composite films will accommodate most of the loaded sulfur. For NCFs, in addition to the lack of mesopores, most of the micropores would be filled with sulfur; consequently, the S/NCF film shows very poor flexibility and cannot afford to fold at all (Fig. S6†). The surface area of S/G/NPCFs sharply decreases to 14 $m^2\ g^{-1}$ after sulfur impregnation; nevertheless, S/G/NPCFs still retain a certain amount of mesopores, which is beneficial for buffering the bending stress and hence maintaining high flexibility for S/G/

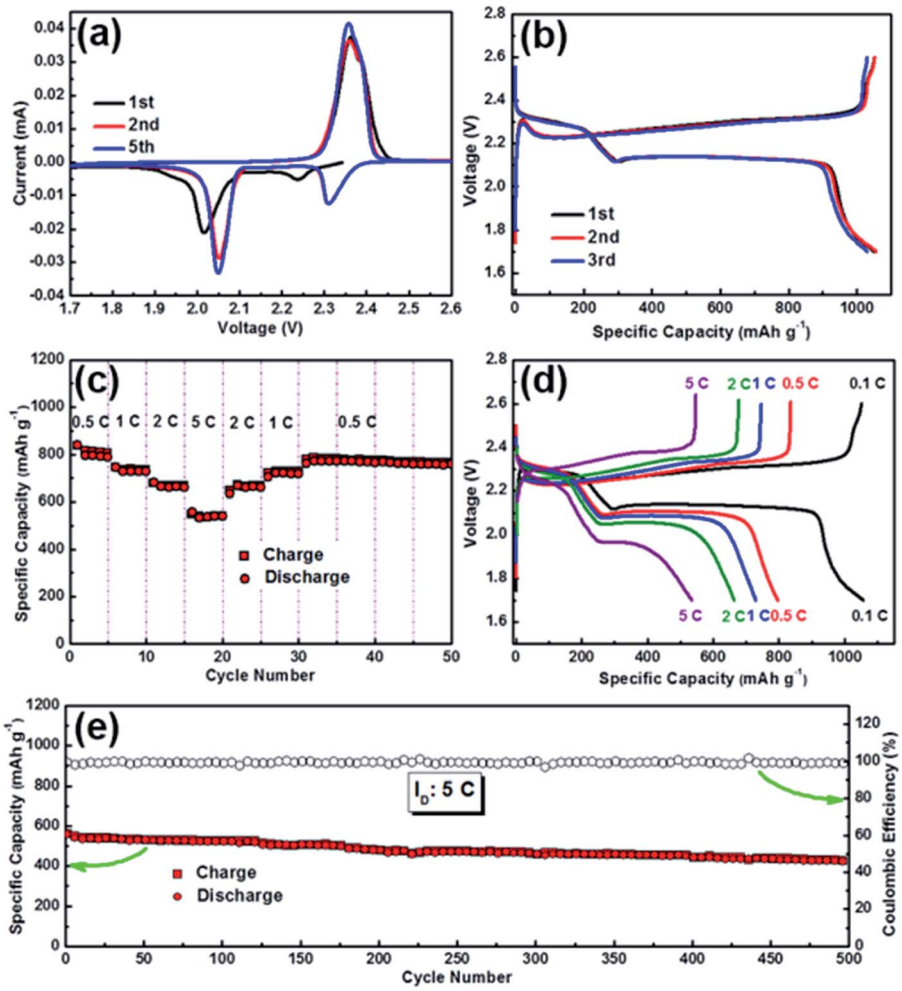

Fig. 3 (a) CV curves for selected cycles of the S/G/NPCF electrode tested at a scan rate of 0.2 mV s^{-1} in the potential range from 1.7 to 2.6 V; (b) typical discharge–charge curves of S/G/NPCFs at 0.1C for the first three cycles; (c) rate capability of the S/G/NPCFs electrode recorded at current rates of 0.5C, 1C, 2C, and 5C; (d) typical discharge–charge curves of S/G/NPCFs at different current densities; (e) long-term cycling performance of S/G/NPCFs at 5C.

NPCFs (Fig. 2d).[49] Due to the large amount of mesopores, the S loading in the S/G/NPCFs reaches 53 wt% (Fig. 2e), which is much higher than those of samples without mesopores (only 40–43 wt%) (Fig. S7†).

The high resolution TEM (HRTEM) images of G/NPCFs (Fig. 2f, S8 and S9†) and S/G/NPCFs (Fig. 2g) demonstrate the presence of highly graphitic carbon as nanoshells (3–5 nm) around the mesopores derived from the SiO_2 template in the nanofibers (as shown with white arrows). The graphitic carbon and mesopores within the nanofibers after sulfur loading are not very obvious due to the interference of the encapsulated sulfur within the nanofibers. In order to exclude the effect of reduced graphene oxide, the TEM and HRTEM images of NPCFs (Fig. S10 and S11†) were studied, which also clearly indicate that graphitic zones exist around the mesopores. In contrast, only amorphous carbon is formed for NCF-based films in the absence of the SiO_2 template.[32,34] The presence of graphitic carbon is further confirmed by the Raman spectra (Fig. 2h). The I_D/I_G value of the samples decreases accordingly upon adding the SiO_2 template regardless of whether there is additionally added reduced graphene oxide or not. The SiO_2/G/NPCFs show the lowest I_D/I_G value, and this is clear evidence for the higher graphitization degree of SiO_2/G/NPCFs than G/NCFs and NCFs. As is widely reported, in addition to its high electrical conductivity, graphitic carbon shows higher mechanical durability than amorphous carbon.[50–52] Therefore, the obtained highly graphitic carbon nanoshells located around mesopores in the nanofibers significantly enhance the mechanical strength and electrical conductivity of the S/G/NPCFs film (Fig. 2b). The result reveals that the rigid SiO_2 template affects the carbonization process of the polymer and catalytically promotes the transformation of amorphous carbon into highly graphitic carbon. The exact "catalysis" mechanism of SiO_2 towards the formation of graphitic carbon is not clear yet, but the present result still sheds light on preparing robust multifunctional graphitic carbon-containing carbonaceous materials/microstructures.

To evaluate the applicability of the free-standing and flexible S/G/NPCFs, the S/G/NPCFs are directly used as a cathode for Li–S batteries. The CV curves of the S/G/NPCF electrode are shown in Fig. 3a. In the first cathodic scan, the reduction peak observed at ~2.24 V is attributed to the change from sulfur to long-chain Li polysulfides,[53] and the reduction peak at ~2.01 V corresponds to the further reduction of higher-order Li polysulfides to Li sulfides.[32] In the following scan, the reduction peaks shift to higher potentials and the oxidation peaks shift to slightly lower potentials compared with the first cycle. This phenomenon should be ascribed to the activation process of the sulfur cathode. The overlap of the 2nd and 5th curves indicates the good reversibility of the electrode. Fig. 3b shows the first three discharge–charge curves of the S/G/NPCF electrode at 0.1C. It presents two voltage plateaus and a high reversible capacity of about 1055 mA h g^{-1} at 0.1C (1C = 1675 mA g^{-1}). As shown in Fig. 3c, the S/G/NPCF electrode exhibits impressive rate capability with a capacity of ~815 mA h g^{-1} at 0.5C and ~540 mA h g^{-1} at 5C, suggesting very fast reaction kinetics. Notably, such an excellent rate performance is rarely reported for Li–S cathode materials (Table S3†). The superior reaction kinetics can be ascribed to the porous composite electrode film decorated with a highly graphitic sp^2 carbon network together with reduced graphene oxide, which not only ensures fast mass diffusion but also efficient charge transfer in the electrode. The corresponding discharge–charge voltage profiles are recorded in Fig. 3d, and the S/G/NPCF electrode maintains relatively obvious charge/discharge plateaus with low overpotentials even at high rates. For example, the overpotential of S/G/NPCFs is only 165 mV at 0.5C and 251 mV at 2C, which is significantly lower than that of S/NPCFs (179 mV at 0.5C and 328 mV at 2C), confirming the good rate performance.[29,54] Notably, due to the low voltage polarization, the S/G/NPCFs show very high energy efficiency (up to 90%) at different current densities, which makes them promising candidates for high-efficiency grid applications (Fig. S12†). The energy density based on the whole electrode reaches as high as 580 W h kg^{-1} at 5C (1095 W h kg^{-1} based on sulfur). For comparison, S/NPCFs without graphene were also tested and showed relatively lower rate capability (Fig. S13†). Moreover, the long-term cycling stability of the S/G/NPCF electrode at 5C was also evaluated (Fig. 3e). The specific capacity was maintained at 427 mA h g^{-1} after 500 cycles, corresponding to a capacity retention of 76.5% of its initial value and a very low capacity decay of 0.047% per cycle. The excellent electrochemical performance of S/G/NPCFs is attributed to the following merits. First, the porous three-dimensional carbon nanofibers provide a self-supported conductive network, which facilitates mass diffusion and charge transfer during lithiation/delithiation reactions. Second, the remaining mesopores in the carbon nanofibers after sulfur loading not only help to buffer the mechanical stress to enhance the flexibility but also accommodate the volume changes during cycling, resulting in

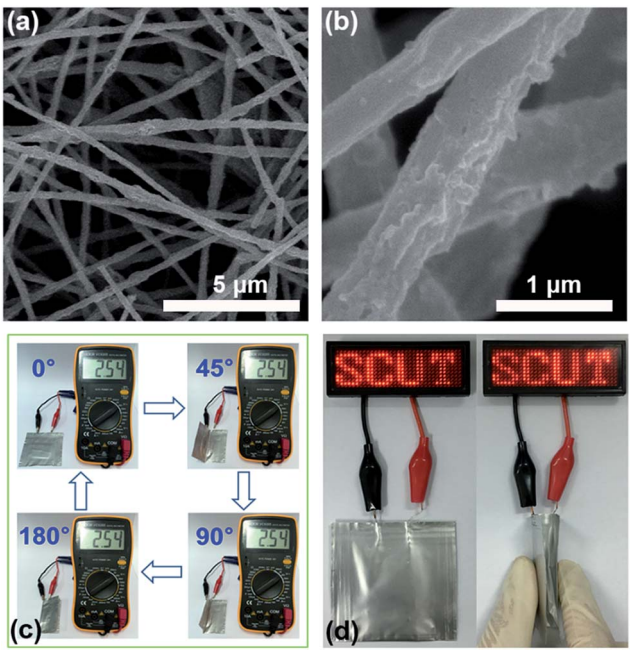

Fig. 4 (a and b) SEM images of S/G/NPCFs after 500 cycles at 5C; (c) the open-circuit voltage of a flexible battery using the S/G/NPCF electrode as the cathode at different bending angles (0–180°); (d) photographs of the LED device lit by the flexible battery during folding.

excellent microstructure stability (Fig. 4a and b). Third, the graphene, high nitrogen-doping and highly graphitic carbon further enhance the electrical conductivity and immobilize polysulfides through strong ionic attraction, which are beneficial for the rate performance and cycling stability.[55]

In order to further confirm the application potential of the S/G/NPCF film for flexible Li–S batteries, a pouch cell with the S/G/NPCF electrode was assembled as a proof of concept. As shown in Fig. 4c, the pouch cell at different bending angles (0°, 45°, 90° and 180°) shows a constant open circuit voltage (OCV), while the OCV of the cell with S/G/NCFs sharply decreases during folding (Fig. S14†). The results demonstrate the stable structure and excellent flexibility of the S/G/NPCFs as a cathode for Li–S batteries. A light emitting diode (LED) device could also be powered by the flexible battery even during the folding process (Fig. 4d), clearly proving the potential of the S/G/NPCF electrode for flexible battery applications.

Conclusions

In summary, a free-standing S/G/NPCF film with high mechanical strength was successfully designed for flexible Li–S batteries. The introduction of a SiO_2 template helps not only to create mesopores but also to improve the graphitization degree of carbon in the nanofibers, both of which play critical roles in their exceeding flexibility and mechanical properties. In addition, the mesopores created in the carbon nanofibers could also help to elevate the sulfur loading. Even after loading the whole electrode with a high content of sulfur (53 wt%), the S/G/NPCF film still exhibited excellent foldability. When directly used as a cathode for a Li–S battery without adding any binder, carbon additive, or metal substrate, the foldable S/G/NPCF electrode exhibited high specific capacity and excellent rate capability. Moreover, a long cycle life of up to 500 cycles at 5C with a decay rate as low as 0.047% per cycle was achieved. Our work has demonstrated a new structural design strategy that can be extended to prepare superior flexible electrodes for high-performance capacitors and other rechargeable batteries.

Acknowledgements

The authors gratefully acknowledge the financial support by the National Natural Science Fund for Distinguished Young Scholars of China (No. 21225625), the National Key Research Program of China (No. 2016YFA0202601), the National Natural Science Foundation of China (No. 21576100 and 21536005), and the Pearl River S&T Nova Program of Guangzhou (201610010062). W. P. Sun acknowledges financial support by ARC DECRA Grant (DE160100596).

References

1 X. Ji and L. F. Nazar, *J. Mater. Chem.*, 2010, **20**, 9821–9826.
2 W. Zhou, X. Xiao, M. Cai and L. Yang, *Nano Lett.*, 2014, **14**, 5250–5256.
3 J. Wang, Y. S. He and J. Yang, *Adv. Mater.*, 2015, **27**, 569–575.
4 P. G. Bruce, S. A. Freunberger, L. J. Hardwick and J.-M. Tarascon, *Nat. Mater.*, 2012, **11**, 19–29.
5 X. Ji, K. T. Lee and L. F. Nazar, *Nat. Mater.*, 2009, **8**, 500–506.
6 Y. Yang, G. Zheng and Y. Cui, *Chem. Soc. Rev.*, 2013, **42**, 3018–3032.
7 Y.-S. Su and A. Manthiram, *Nat. Commun.*, 2012, **3**, 1166.
8 D.-W. Wang, Q. Zeng, G. Zhou, L. Yin, F. Li, H.-M. Cheng, I. R. Gentle and G. Q. M. Lu, *J. Mater. Chem. A*, 2013, **1**, 9382–9394.
9 Z. Li, J. Zhang, B. Guan, D. Wang, L.-M. Liu and X. W. (David) Lou, *Nat. Commun.*, 2016, **7**, 13065.
10 R. Fang, S. Zhao, P. Hou, M. Cheng, S. Wang, H. M. Cheng, C. Liu and F. Li, *Adv. Mater.*, 2016, **28**, 3374–3382.
11 H. Wang, W. Zhang, H. Liu and Z. Guo, *Angew. Chem., Int. Ed.*, 2016, **55**, 3992–3996.
12 Z. Li, J. T. Zhang, Y. M. Chen, J. Li and X. W. (David) Lou, *Nat. Commun.*, 2015, **6**, 8850.
13 W. Li, H. Yao, K. Yan, G. Zheng, Z. Liang, Y.-M. Chiang and Y. Cui, *Nat. Commun.*, 2015, **6**, 7436.
14 J. Wang, Z. Yao, C. W. Monroe, J. Yang and Y. Nuli, *Adv. Funct. Mater.*, 2013, **23**, 1194–1201.
15 H. Wang, V. Sencadas, G. Gao, H. Gao, A. Du, H. Liu and Z. Guo, *Nano Energy*, 2016, **26**, 722–728.
16 J. A. Rogers, T. Someya and Y. Huang, *Science*, 2010, **327**, 1603–1607.
17 M. J. Cima, *Nat. Biotechnol.*, 2014, **32**, 642–643.
18 T. Cheng, Y. Zhang, W. Y. Lai and W. Huang, *Adv. Mater.*, 2015, **27**, 3349–3376.
19 G. Zhou, F. Li and H.-M. Cheng, *Energy Environ. Sci.*, 2014, **7**, 1307–1338.
20 X. F. Wang, X. H. Lu, B. Liu, D. Chen, Y. X. Tong and G. Z. Shen, *Adv. Mater.*, 2014, **26**, 4763–4782.
21 L. Li, Z. Wu, S. Yuan and X.-B. Zhang, *Energy Environ. Sci.*, 2014, **7**, 2101–2122.
22 M. Yousaf, H. T. H. Shi, Y. S. Wang, Y. J. Chen, Z. M. Ma, A. Y. Cao, H. E. Naguib and R. P. S. Han, *Adv. Energy Mater.*, 2016, **6**, 1600490.
23 Z. Yuan, H.-J. Peng, J.-Q. Huang, X.-Y. Liu, D.-W. Wang, X.-B. Cheng and Q. Zhang, *Adv. Funct. Mater.*, 2014, **24**, 6105–6112.
24 H.-J. Peng, W.-T. Xu, L. Zhu, D.-W. Wang, J.-Q. Huang, X.-B. Cheng, Z. Yuan, F. Wei and Q. Zhang, *Adv. Funct. Mater.*, 2016, **26**, 6351–6358.
25 G. Zhou, L. Li, C. Ma, S. Wang, Y. Shi, N. Koratkar, W. Ren, F. Li and H.-M. Cheng, *Nano Energy*, 2015, **11**, 356–365.
26 H. S. Kang and Y. K. Sun, *Adv. Funct. Mater.*, 2016, **26**, 1225–1232.
27 L. Sun, D. Wang, Y. Luo, K. Wang, W. Kong, Y. Wu, L. Zhang, K. Jiang, Q. Li and Y. Zhang, *ACS Nano*, 2015, **10**, 1300–1308.
28 H. Chen, C. Wang, Y. Dai, S. Qiu, J. Yang, W. Lu and L. Chen, *Nano Lett.*, 2015, **15**, 5443–5448.
29 G. Zhou, L. Li, D. W. Wang, X. Y. Shan, S. Pei, F. Li and H. M. Cheng, *Adv. Mater.*, 2015, **27**, 641–647.
30 D. Nan, Z.-H. Huang, R. Lv, L. Yang, J.-G. Wang, W. Shen, Y. Lin, X. Yu, L. Ye and H. Sun, *J. Mater. Chem. A*, 2014, **2**, 19678–19684.

31 H.-G. Wang, S. Yuan, D.-L. Ma, X.-B. Zhang and J.-M. Yan, *Energy Environ. Sci.*, 2015, **8**, 1660–1681.
32 L. Ji, M. Rao, S. Aloni, L. Wang, E. J. Cairns and Y. Zhang, *Energy Environ. Sci.*, 2011, **4**, 5053–5059.
33 L. Zeng, Y. Jiang, J. Xu, M. Wang, W. Li and Y. Yu, *Nanoscale*, 2015, **7**, 10940–10949.
34 L. Zeng, F. Pan, W. Li, Y. Jiang, X. Zhong and Y. Yu, *Nanoscale*, 2014, **6**, 9579–9587.
35 L. Sun, D.-T. Wang, Y.-F. Luo, K. Wang, W.-B. Kong, Y. Wu, L.-N. Zhang, K.-L. Jiang, Q.-Q. Li, Y.-H. Zhang, J.-P. Wang and S.-S. Fan, *ACS Nano*, 2016, **10**, 1300–1308.
36 J.-Q. Huang, H.-J. Peng, X.-Y. Liu, J.-Q. Nie, X.-B. Cheng, Q. Zhang and F. Wei, *J. Mater. Chem. A*, 2014, **2**, 10869–10875.
37 L. Zhu, H.-J. Peng, J.-Y. Liang, J.-Q. Huang, C.-M. Chen, X.-F. Guo, W.-C. Zhu, P. Li and Q. Zhang, *Nano Energy*, 2015, **11**, 746–755.
38 L. Sun, W.-B. Kong, Y. Jiang, H.-C. Wu, K.-L. Jiang, J.-P. Wang and S.-S. Fan, *J. Mater. Chem. A*, 2015, **3**, 5305–5312.
39 P. Lian, X. Zhu, S. Liang, Z. Li, W. Yang and H. Wang, *Electrochim. Acta*, 2010, **55**, 3909–3914.
40 M. Jing, C.-G. Wang, B. Zhu, Y.-X. Wang, X.-P. Gao and W.-N. Chen, *J. Appl. Polym. Sci.*, 2008, **108**, 1259–1264.
41 X.-H. Qin, *J. Therm. Anal. Calorim.*, 2010, **99**, 571–575.
42 R. Andrews, D. Jacques, D. Qian and E. C. Dickey, *Carbon*, 2001, **39**, 1681–1687.
43 Q. Pang, J. T. Tang, H. Huang, X. Liang, C. Hart, K. C. Tam and L. F. Nazar, *Adv. Mater.*, 2015, **27**, 6021–6028.
44 G. M. Zhou, E. Paek, G. S. Hwang and A. Manthiram, *Nat. Commun.*, 2015, **6**, 7760.
45 X.-Q. Niu, X.-L. Wang, D. Xie, D.-H. Wang, Y.-D. Zhang, Y. Li, T. Yu and J.-P. Tu, *ACS Appl. Mater. Interfaces*, 2015, **7**, 16715–16722.
46 C. Wang, X. S. Wang, Y. J. Wang, J. T. Chen, H. H. Zhou and Y. H. Huang, *Nano Energy*, 2015, **11**, 678–686.
47 P. Zhu, J. Song, D. Lv, D. Wang, C. Jaye, D. A. Fischer, T. Wu and Y. Chen, *J. Phys. Chem. C*, 2014, **118**, 7765–7771.
48 J. X. Song, M. L. Gordin, T. Xu, S. R. Chen, Z. X. Yu, H. Sohn, J. Lu, Y. Ren, Y. H. Duan and D. H. Wang, *Angew. Chem., Int. Ed.*, 2015, **127**, 4399–4403.
49 Y. M. Sun, R. B. Sills, X. L. Hu, Z. W. Seh, X. Xiao, H. H. Xu, W. Luo, H. Y. Jin, Y. Xin, T. Q. Li, Z. L. Zhang, J. Zhou, W. Cai, Y. H. Huang and Y. Cui, *Nano Lett.*, 2015, **15**, 3899–3906.
50 D. A. Dikin, S. Stankovich, E. J. Zimney, R. D. Piner, G. H. B. Dommett, G. Evmenenko, S. T. Nguyen and R. S. Ruoff, *Nature*, 2007, **448**, 457–460.
51 G. M. Zhou, S. F. Pei, L. Li, D.-W. Wang, S. G. Wang, K. Huang, L.-C. Yin, F. Li and H.-M. Cheng, *Adv. Mater.*, 2014, **26**, 625–631.
52 M.-Q. Zhao, Q. Zhang, J.-Q. Huang, G.-L. Tian, J.-Q. Nie, H.-J. Peng and F. Wei, *Nat. Commun.*, 2014, **5**, 3410.
53 S. Evers and L. F. Nazar, *Acc. Chem. Res.*, 2012, **46**, 1135–1143.
54 H. Hu, H. Cheng, Z. Liu, G. Li, Q. Zhu and Y. Yu, *Nano Lett.*, 2015, **15**, 5116.
55 J. Zhang, C.-P. Yang, Y.-X. Yin, L.-J. Wan and Y.-G. Guo, *Adv. Mater.*, 2016, **28**, 9539–9544.